

1                    **Novel ductile wellbore cementitious composite for geologic CO<sub>2</sub> storage**

2  
3                    Jubilee T. Adeoye, Duo Zhang, Victor C. Li, and Brian R. Ellis\*

4                    Department of Civil and Environmental Engineering, University of Michigan

5                    \*Correspondence: [brellis@umich.edu](mailto:brellis@umich.edu); 734-763-5470

6  
7                    **ABSTRACT**

8 CO<sub>2</sub> leakage through damaged wellbore cement sheaths is a major risk of geologic CO<sub>2</sub> storage  
9 (GCS), as conventional wellbore cement is brittle and can be damaged due to acid attack and  
10 downhole stresses during CO<sub>2</sub> injection. Here we examine a novel fiber-reinforced engineered  
11 cementitious composite (ECC) proposed as a substitute to conventional wellbore cement due to  
12 its superior ductility and intrinsic crack width control. ECC and conventional wellbore cement  
13 coupons were exposed to water in equilibrium with CO<sub>2</sub> at 50°C and 10 MPa. The samples were  
14 retrieved after several days and their mechanical performance was evaluated using a four-point  
15 bending test, microhardness, and compressive strength analyses. Optical microscopy and  
16 mercury intrusion porosimetry were used to characterize the progression of the carbonation front  
17 and pore structures of the specimens. Control experiments were conducted under the same  
18 temperature and pressure conditions but with a N<sub>2</sub> headspace to isolate the impact of CO<sub>2</sub>. It was  
19 found that carbonation increased the ultimate flexural strength of ECC but decreased its ductility.  
20 However, the ductility of carbonated ECC remained higher than that of conventional wellbore  
21 cements that exhibited brittle failure under all test conditions. Additionally, ECC exhibited  
22 minimal material loss and continued resistance to deformation in comparison to conventional  
23 wellbore cements. This suggests that while the exposure of ECC to CO<sub>2</sub> will alter its mechanical  
24 properties, altered ECC will continue to exhibit mechanical performance superior to  
25 conventional wellbore cement, and therefore shows promise as a highly durable wellbore  
26 cementing material for GCS applications.

27  
28                    **Keywords:** Geologic CO<sub>2</sub> storage; wellbore cement sheath; Mechanical integrity; CO<sub>2</sub> leakage  
29                    mitigation; Engineered cementitious composite

## 32 1. Introduction

33

34 Geologic CO<sub>2</sub> storage (GCS) has been identified as a bridging technology to slow global  
35 climate change due to its ability to stabilize the atmospheric concentration of CO<sub>2</sub> by eliminating  
36 large streams of the greenhouse gas (IPCC and Metz, 2005). However, leakage of stored CO<sub>2</sub>  
37 from geologic reservoirs through damaged or abandoned wells remains a major risk of adopting  
38 GCS as a long-term strategy to slow global climate change (Bachu and Celia, 2009; Chow et al.,  
39 2003; Deel, 2007; Nordbotten et al., 2009, 2005; Watson and Bachu, 2009). Wellbore pathways  
40 through which CO<sub>2</sub> can leak from geologic reservoirs have been well documented, and include  
41 fractured cement sheaths, damaged steel casing, and steel casing/cement and cement/formation  
42 annular gaps (Bachu and Celia, 2009; Carroll et al., 2016). In particular, leakage of CO<sub>2</sub> through  
43 fractured cement sheaths is a major concern as conventional wellbore cementing materials are  
44 made of Portland cement, a brittle material that can be damaged by stresses generated during  
45 CO<sub>2</sub> injection and cyclic thermal swings (Nelson, 1990; Roy et al., 2018).

46 Previous studies that investigated the long-term effect of exposing wellbore cement to CO<sub>2</sub>  
47 have shown that the risks of cement sheath damage increase following carbonation and the  
48 overall mechanical strength of cement will be compromised following exposure to CO<sub>2</sub> under  
49 GCS conditions (Barlet-Gouédard et al., 2007; Fabbri et al., 2009; Li et al., 2015). Barlet-  
50 Gouédard et al. (2007) reported a 65% and 30% loss of bulk compressive strength in Portland  
51 cement exposed to CO<sub>2</sub>-acidified water and wet supercritical CO<sub>2</sub>, respectively, for six weeks at  
52 temperature and pressure conditions of 90°C and 28 MPa. The exposure of the cement to CO<sub>2</sub>  
53 also led to damage and degradation characterized by spalling and cracking. In the study carried  
54 out by Li et al. (2015) on Portland cement coupons exposed to CO<sub>2</sub>-acidified brine at  
55 temperature and pressure conditions of 95°C and 10 MPa, three-point bending test and  
56 nanoindentation analysis were carried out on the coupons to investigate the effect of CO<sub>2</sub> on both  
57 the overall flexural and microstructural strength of the cement. Significant reduction in the  
58 overall flexural strength and modulus of elasticity was observed in samples exposed to CO<sub>2</sub> in  
59 comparison to control samples exposed to nitrogen headspace under similar temperature and  
60 pressure conditions. Fabbri et al. (2009) reported deterioration of the in-situ hydro-mechanical  
61 properties of Portland cement cores after several weeks of exposure to CO<sub>2</sub> at temperature and  
62 pressure conditions of 90°C and 28 MPa. This alteration led to an increase in the permeability of

63 the cement cores, potentially increasing the risk of CO<sub>2</sub> leakage. Because the integrity of  
64 wellbore cement sheath is crucial for CO<sub>2</sub> storage security during GCS, there is a need to ensure  
65 that materials used in wellbore cementing can withstand the cyclic stresses induced during CO<sub>2</sub>  
66 injection, which are variable but can be in excess of 25 MPa (Jen et al., 2017; Rutqvist et al.,  
67 2007), and limit the extent of cement sheath damage under such conditions.

68 Engineered cementitious composite (ECC), a class of fiber-reinforced cementitious  
69 composites, is being proposed here as a possible candidate for wellbore cementing during GCS.  
70 ECC exhibits high tensile ductility, which is the capacity to undergo large tensile deformations  
71 before rupture, instead of brittle failure observed in conventional wellbore cement. ECC also  
72 shows strain-hardening behavior, which is the ability to bare more load at higher deformation  
73 through forming multiple fine cracks, typically less than 60 μm, at the microscale (Kan et al.,  
74 2010; Li, 2003). Studies have shown that ECC has a tensile strain capacity in the range of 2 to  
75 5%, which is 200 to 500 times that of Portland cement and concrete (Li, 2009, 2003). Because  
76 tight cracks in conventional wellbore cement have been shown to heal autogenously when in  
77 contact with CO<sub>2</sub>-rich fluids (Cao et al., 2015; Carroll et al., 2016; Huerta et al., 2016) in  
78 comparison to larger cracks, the ability of ECC to maintain cracks typically less than 60 μm  
79 during the stain hardening stage makes it an attractive candidate for wellbore cementing  
80 applications during GCS.

81 In a recent study carried out by Adeoye et al. (2019) on conventional M45 ECC exposed to  
82 CO<sub>2</sub>-saturated water at P<sub>CO2</sub> of 10 MPa and temperature of 50°C, an increase in microhardness  
83 was observed in all regions of the composite following reaction with CO<sub>2</sub>. The increase in  
84 hardness was attributed to pore refinement in the ECC matrix, due to continuous pozzolanic  
85 reactions, and reworking of parent cementitious material into a denser matrix following  
86 carbonation. Such pore refinement and reworked matrix has been reported by Cheshire et al.  
87 (2017) in cement cores recovered from an injection well in a CO<sub>2</sub>-enhanced oil recovery field in  
88 West Texas, and can improve the resistance of the material to deformation and reduce fluid  
89 permeability through the composite. Adeoye et al. (2019) also observed that the fiber/matrix  
90 interfacial transition zone (ITZ) in the M45 ECC was densified with reaction products that were  
91 identified as calcium carbonate after exposure to CO<sub>2</sub>. Such densification of the ITZ could  
92 impact the ductility, long-term strain hardening property, and multiple cracking behavior of  
93 ECC, as the denser ITZ will increase the bonding between fibers and matrix, potentially

94 promoting rupturing of fibers rather than pullout under tensile stress (Li et al., 2002; Li, 2003;  
95 Redon et al., 2001). To determine the suitability of ECC as substitute for conventional wellbore  
96 cementing materials in injection wells during GCS, it is important to understand how the  
97 ductility and mechanical integrity of ECC will be impacted by reaction with CO<sub>2</sub> under typical  
98 GCS conditions.

99 This work investigates the changes in the mechanical properties of an ECC material  
100 formulated for wellbore cementing applications in order to predict its long-term integrity  
101 following exposure to CO<sub>2</sub> under typical GCS conditions. A series of static batch experiments  
102 were carried out, simulating diffusive mass flow conditions expected in wellbore cement sheath,  
103 and a four-point flexural test was used to determine the impact of CO<sub>2</sub> on the ductility of ECC in  
104 comparison to conventional wellbore cements. The evolution of ECC microstructure was also  
105 characterized to provide insight regarding the factors that will impact the overall mechanical  
106 performance of ECC during GCS.

107

## 108 **2. Materials and methods**

109

### 110 **2.1. Material selection**

111

112 ECC material selection was carried out to achieve a fresh state mix with flow properties that  
113 are more representative of a wellbore cement slurry in comparison to standard M45 ECC (See  
114 Supporting Information) (Guillot, 1990; Li, 2009; Nelson et al., 1990). Silica sand used in  
115 standard M45 ECC was replaced with low calcium content Class F fly ash (ASTM C618, Type  
116 F) to improve the flowability of the mix in the fresh state. The chemical composition of the fly  
117 ash used is presented in **Table 1**. Type III cement, which is early-strength cement, was used for  
118 the ECC mix instead of Class H wellbore cement to compensate for the negative effect of high  
119 fly ash content and water to cement ratio on early age strength development. Type III cement is  
120 able to develop early age strength faster than Class H wellbore cement because of its higher  
121 surface area (5000 m<sup>2</sup>/kg) in comparison to Class H wellbore cement (1600 m<sup>2</sup>/kg) and higher Al-  
122 phase content (Michaux et al., 1990). A fly ash: cement ratio of 50:50 by weight, which is a  
123 typical wellbore comment slurry blend, was used for specimen preparation in this study (Nelson  
124 et al., 1990). REC 15 polyvinyl alcohol (PVA) fiber with a length of 8 mm and 0.5% oil coating

125 supplied by Kuraray Ltd. (Japan) was chosen over the 12 mm fiber used in standard M45 ECC  
 126 because shorter fibers promote more uniform fiber dispersion in a low-viscosity mix. The  
 127 physical and mechanical properties of the PVA fibers are presented in **Table 2**. In this study, we  
 128 have used a 1.1% fiber volume, which is considerably less than the 2% fiber volume used in  
 129 conventional ECC (Li, 2009). This is because the lower volume promoted adequate dispersion of  
 130 fibers in the slurry. Anti-settling agent was added to prevent free water by promoting gelation in  
 131 the fresh mixture and a dispersant was added for viscosity control. Samples were mixed using tap  
 132 water. For the sake of brevity, this version of ECC is labeled in this paper as WECC (wellbore  
 133 ECC). Reference samples representing conventional wellbore cement were prepared using Class  
 134 H cement.

135

136 **Table 1:** Chemical composition of fly ash.

Chemical Composition.	SiO <sub>2</sub>	Al <sub>2</sub> O <sub>3</sub>	Fe <sub>2</sub> O <sub>3</sub>	SO <sub>3</sub>	CaO	MgO	Na <sub>2</sub> O	K <sub>2</sub> O	LOI*
%	51.8	20.6	14.8	0.8	4.1	1.0	1.3	2.4	2.80

137 \*LOI is loss on ignition

138

139 **Table 2:** Physical and mechanical properties of PVA fibers used in WECC.

Length (mm)	Diameter ( $\mu$ m)	Density (kg/m <sup>3</sup> )	Tensile strength (MPa)	Elongation (%)	Young's Modulus (GPa)
8	39	1.3	1600	7	42

140

## 141 2.2. Sample preparation

142 Three sets of samples were prepared with the mix proportions presented in **Table 3**. WECC  
 143 represents the composition of ECC proposed for wellbore cementing applications during GCS.  
 144 Fiber-free WECC (hereafter referred to as FFWECC) has the same composition as WECC, but  
 145 the fibers have been excluded from the mix to isolate the unique impact of the fibers on the  
 146 microstructural behavior of WECC under GCS conditions. Thus, FFWECC is comparable to  
 147 conventional fly ash-amended wellbore cement (Kutchko et al., 2009; Zhang et al., 2014). Class  
 148 H composition is the conventional wellbore cementing material (Nelson et al., 1990). Both  
 149 FFWECC and Class H served as benchmarks to evaluate the mechanical performance of WECC.  
 150 For WECC, the solid components were dry-mixed at 200 rpm for 5 mins. A premixed solution  
 151 containing the liquid components was then added to the mix over the course of 5 mins.

152 Subsequently, PVA fibers were added to the slurry over a period of 2.5 mins, mixed at a constant  
 153 rate of 200 rpm. The slurry was further mixed after the addition of the fibers for an additional 2.5  
 154 mins to ensure uniform fiber dispersion. FFW ECC was prepared using a similar approach as  
 155 WECC, but the fiber addition process was excluded. For Class H cement, the cement was mixed  
 156 for 3 mins followed by addition of the premixed liquid components for 5 mins. All samples were  
 157 prepared using a 6-liter countertop mixer (KitchenAid). The fresh slurries were cast in  
 158 customized Plexiglas rectangular coupon molds (102 mm x 34 mm x 10 mm) shown in Fig. 1a to  
 159 generate several specimens for flexural testing, and in 2-inch cubic molds prepared according to  
 160 ASTM standard C109 for compressive strength analysis of cement mortars (ASTM, 2016). The  
 161 specimens were placed in a curing chamber (Temp. =  $22 \pm 2^\circ\text{C}$  and RH =  $99 \pm 1\%$ ) and  
 162 demolded 24 hours after casting. The samples were then cured under this condition for 28 days.

163

164 **Table 3:** Composition of materials. Water content is reported as a fraction of the total solid  
 165 weight WCEE: wellbore ECC; FFW ECC: fiber-free WECC; Class H: conventional wellbore  
 166 cement.

Sample Type	Solid Phase		Liquid Phase	Fiber vol. (%)
	Cement	Fly ash	Water	
WECC	0.5	0.5	0.45	1.1
FFWECC	0.5	0.5	0.45	0
Class H	1	0	0.38	0

167 Note: Additives including dispersant, antifoam, and antisetling agents were added to  
 168 modify slurry fresh state flow properties.

169

### 170 2.3. Static batch experiments

171

172 Eight WECC/FFWECC, and six Class H cement samples were placed in 600 mL batch  
 173 reactors filled with 300 mL of deionized water with a resistivity greater than 18.2 M $\Omega$ -cm such  
 174 that the samples were fully submerged (**Fig. 1b**). Pure water was used in this study to ensure that  
 175 the samples were exposed to the most acidic environment under the chosen temperature and P<sub>CO2</sub>  
 176 conditions (Rimmelé et al., 2008; Spycher and Pruess, 2005). The temperature and P<sub>CO2</sub> in the  
 177 batch reactors were subsequently elevated to 50°C and 10 MPa, respectively. For WECC and  
 178 FFW ECC, two samples were retrieved from each reactor after 2, 7, 14, and 28 days, while Class

179 H cement samples were retrieved after 2, 7, and 21 days. For each pair of samples retrieved  
 180 from the reactor, the samples were replaced with two Teflon coupons of the same dimensions.  
 181 This ensured a constant water level in the batch reactor throughout the experiment, such that the  
 182 samples were completely submerged in water at all times, without needing to add additional  
 183 water to the reactor. Similarly, two 2-inch cubic specimens of each sample type were exposed to  
 184 CO<sub>2</sub>-acidified water under the same temperature and pressure conditions and retrieved after 7  
 185 days of reaction.

186 To decouple the effect of elevated temperature and pressure conditions from the unique  
 187 interactions between WECC and CO<sub>2</sub>, a control experiment was set up in which the coupons  
 188 were exposed similarly to a N<sub>2</sub> headspace with P<sub>N<sub>2</sub></sub> of 10 MPa and temperature of 50°C. The  
 189 headspace in the batch reactor was purged with nitrogen prior to starting the experiment to  
 190 eliminate ambient air containing CO<sub>2</sub> from the reactor. After retrieving the samples from the  
 191 reactor, they were air-dried at room temperature conditions (23± 2°C) for 24 hours to expel  
 192 surficial water before carrying out the four-point bending flexural test.

193

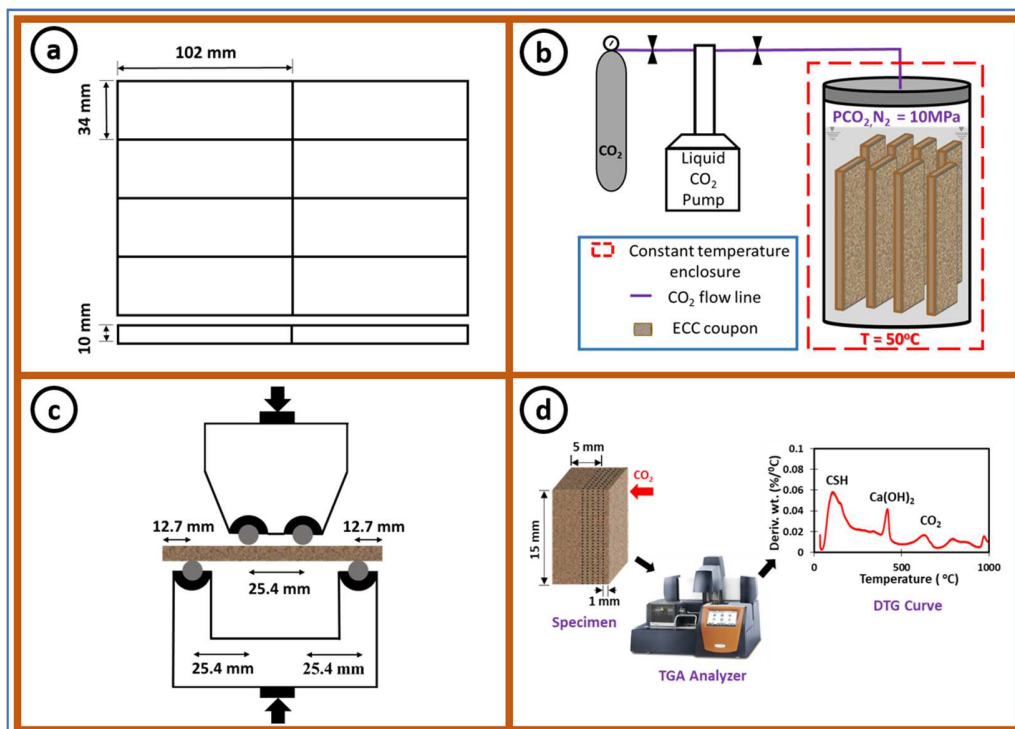


**Fig. 1:** Experimental procedures for the study. (a) Customized mold for coupon specimens. Dimensions were chosen to maintain a coupon span to height ratio of 10:1. (b) Experimental setup for the batch study. Temperature and pressure were kept constant throughout the study. Coupons specimens were replaced with dummy Teflon coupons after sample retrieval. (c) Customized setup for four-point bending test. Top and bottom sections of the test cell were cut out of a single piece aluminum block and steel dowels were used as rollers. (d) Flow diagram for TGA analysis.

## 194 **2.4. Sample analysis**

195

### 196 **2.4.1 Four-point bending test**

197

198 A four-point bending test was carried out to determine the ductility and ultimate flexural  
199 strength of the specimens, pre- and post-reaction with CO<sub>2</sub>, using an Instron mechanical test  
200 frame equipped with Bluehill software (Instron) for actuator control and data acquisition. The  
201 sample stage was custom-made using single-piece aluminum frames for the upper and lower  
202 supports, with steel dowels used as rollers, as shown in **Fig. 1c**. The coupons were pre-loaded to  
203 20 N and subsequently loaded at a constant displacement rate of 0.1 mm/min. The loading rate  
204 was maintained until the load dropped below 50% of the maximum load sustained by the sample.  
205 The flexural stress ( $\sigma_f$ ) of the coupons was determined using the expression:

$$206 \quad \sigma_f = \frac{Fl}{bd^2} \quad (1)$$

207

208 where  $F$  is the loading force (N),  $l$  is the distance between the two supporting pins (mm),  $b$  is  
209 the width of the coupon (mm), and  $d$  is the thickness of the sample (ASTM, 2012). The  
210 modulus of rupture ( $\sigma_{fmax}$ ) was computed based on the peak value of  $F$ .

211

### 212 **2.4.2 Microhardness and compressive strength analyses**

213

214 Microhardness analysis was carried out to determine the variation in local micromechanical  
215 strength and resistance to deformation of the different regions of the sample following acid  
216 attack. Samples were polished using a series of finer sandpaper grit sizes with a final finish  
217 achieved using a P2400-grit sandpaper and the test was carried out using a Vickers hardness  
218 tester (LECO). The altered and unaltered regions of the coupons were segmented into different  
219 zones, with more data points obtained from the edge of the sample in contact with CO<sub>2</sub>-acidified  
220 water (Adeoye et al., 2019; Zhang et al., 2014). This ensured higher resolution of the  
221 microhardness measured along the most altered region of the core. The test used a loading force  
222 of 500 g and a dwell time of 10 seconds. The microhardness of each zone was reported as a  
223 hardness value (HV) for a 500 g load based on the average hardness of 12 indents, with higher  
224 HV indicating greater resistance of the material to deformation (Dieter and Bacon, 1986).

225 Compressive strength analysis was carried out on the carbonated and unaltered 2-inch cubes  
226 using a Forney compression machine (Forney). The initial load of 5 N was applied to the load  
227 cell and a constant loading rate of 3 N/s was applied until the peak load was attained. The test  
228 was stopped after the load dropped to 75% of the peak load. The compressive strength of the  
229 samples was then determined using the expression:

$$230 \quad F_m = \frac{P}{A} \quad (2)$$

231 Where  $F_m$  is the compressive strength in MPa,  $P$  is the total maximum load in N, and  $A$  is the  
232 area of loaded surface mm<sup>2</sup> (ASTM, 2016).

233

### 234 **2.4.3 Extent of carbonation alteration**

235

236 To determine the extent of alteration and carbonation of the samples following reaction with  
237 CO<sub>2</sub>, each coupon was sectioned using a saw and the sectioned surface was stained with  
238 phenolphthalein pH indicator to determine the carbonated and uncarbonated regions based on the  
239 variation in the pH along the reaction front. The depth of the altered zone was estimated by  
240 taking the average of 10 measurements from the edge of the coupon to the edge of the altered  
241 zone (i.e., region of reduced pH). To further compare the structural change and material loss  
242 along the edge of the sample following reaction with CO<sub>2</sub> in WECC and FFWECC, optical  
243 microscopy was carried out on the polished surface of the sectioned specimens using a Nikon  
244 LV100ND optical microscope (Nikon Instruments Inc.) equipped with a 5x magnification lens.

245

### 246 **2.4.4 Mercury intrusion porosimetry**

247

248 Quantitative changes in the porosity and pore size distribution of the specimens were  
249 determined using mercury intrusion porosimetry (MIP). Samples were cut into ~30 mm<sup>3</sup> sections  
250 and dewatered via solvent replacement by soaking in isopropanol for 7 days (Feldman, 1987;  
251 Gallé, 2001). Specimens were subsequently vacuum-dried in a desiccator at ambient temperature  
252 conditions for 72 hours. The samples were then analyzed in 5 cm<sup>3</sup> penetrometers using a  
253 MicroActive AutoPore V 9600 mercury intrusion porosimeter (Micromeritics Instrument  
254 Corporation) with maximum injection pressure of 421 MPa.

255

#### 256 **2.4.5 Thermogravimetric analysis**

257

258 Thermogravimetric analysis (TGA) was used to quantify the hydrated products in WECC and  
259 FFWECC samples at different depths along the reaction front after exposure to CO<sub>2</sub> acidified  
260 water. This was done to investigate the differences in the evolution of WECC carbonation  
261 products relative to FFWECC and to chemically investigate if the fibers will alter the  
262 carbonation trends observed in conventional fly ash-amended wellbore cement. 15 mm x 5 mm  
263 x 10 mm sections of the coupons were obtained and each sample was sanded at 1 mm intervals  
264 along the reaction front toward the center of the coupon as described in **Fig. 1d**. The 1 mm  
265 section represents the section of the sample in direct contact with CO<sub>2</sub> acidified water. Samples  
266 were analyzed using a thermogravimetric analyzer (TA Instruments, SDT 650). 20 mg of each  
267 specimen was placed in a 90 µl aluminum crucible and the temperature was ramped up to 35°C  
268 at a rate of 1°C/ min, and held constant for 60 min to eliminate free water (Neves Junior et al.,  
269 2019). The temperature was subsequently ramped up to 1000°C at a rate of 10°C per minute.

270

### 271 **3. Results and discussion**

272

#### 273 **3.1 Long-term alteration of WECC**

274

275 **Fig. 2a** presents depth of carbonation at different time points for WECC and FFWECC,  
276 obtained by staining the cross section of the specimens with phenolphthalein pH indicator prior  
277 before and after exposure to CO<sub>2</sub>. The clear and pink regions of the stained surfaces represent the  
278 altered and unaltered sections of the coupons, respectively (RILEM, 1984; Verbeck, 1958;  
279 Zhang and Shao, 2016). The result indicates that the average depth of carbonation for WECC  
280 and FFWECC after two days of reaction was  $1.42 \pm 0.17$  mm and  $1.41 \pm 0.15$  mm, respectively.  
281 Both WECC and FFWECC samples were fully reacted after 28 days of reaction. The fact that the  
282 carbonation depths were comparable for both WECC and FFWECC at different time points  
283 suggests that the presence of fibers did not promote deeper penetration of CO<sub>2</sub> into the ECC  
284 matrix  
285 and will therefore not enhance the extent of carbonation under GCS conditions.

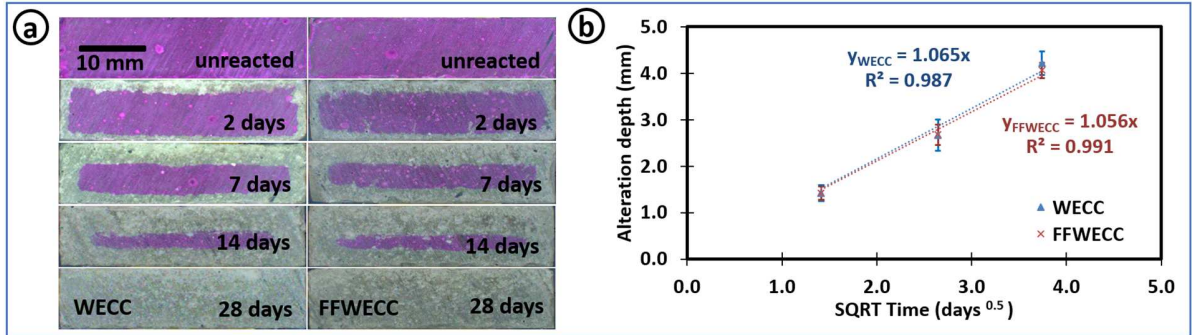


**Fig. 2:** (a) Alteration front of reacted and unreacted WECC and FFWGCC specimens using phenolphthalein pH indicator. Pink and clear regions are the uncarbonated and carbonated regions of the samples, respectively. (b) Combined plot of the alteration depth vs. SQRT time for WECC and FFWGCC using phenolphthalein pH indicator. Equations  $Y_{WECC}$  and  $Y_{FFWGCC}$  describe the extent of carbonation for WECC and FFWGCC, respectively, as a function of time using phenolphthalein pH indicator. Error bars represent the standard deviation of 10 measurements of the altered depth from the edge of the coupon to the leading edge of the alteration zone. The goodness of linear fit of the alteration depth vs. square root (SQRT) of time indicates that  $CO_2$  transport in WECC and FFWGCC is a diffusion-controlled process.

286

287 **Fig. 3.2b** plots alteration depth as a function of square root of time, which describes the  
 288 extent of carbonation according to Fick's second law of diffusion and is typically used to  
 289 estimate the rate of carbonation of cement in systems under constant concentration boundary  
 290 conditions (Neville, 2011). The results show that the early time alteration of the WECC and  
 291 FFWGCC follow

292 linear trends with  $R_{WECC} = 0.98$  and  $R_{FFWGCC} = 0.99$  (**Fig 2b**). Based on this correlation,  $CO_2$   
 293 penetration through WECC and FFWGCC at different time points was shown to be a diffusive  
 294 process according to:

295

$$296 \quad Y_{WECC} = 1.065x \quad (3)$$

297

$$298 \quad Y_{FFWGCC} = 1.056x \quad (4)$$

299

300 where  $Y_{WECC}$ ,  $Y_{FFWGCC}$  are the depths of alteration in mm for ECC and FFWGCC, respectively,  
 301 and  $x$  is the square root of time in days<sup>1/2</sup>. Based on equations (3) and (4), the estimated extent of  
 302 carbonation for the WECC and FFWGCC samples after 28 days of exposure to  $CO_2$  acidified

303 water will be 5.63 and 5.58 mm, respectively. This is consistent with the observation in the 28-  
304 day samples that showed that the 10 mm thick samples had been fully reacted, as the carbonation  
305 progressed from all sides of the rectangular specimens.

306 In contrast to the WECC and FWECC samples in which significant carbonation was  
307 observed after reaction with CO<sub>2</sub>, the Class H cement samples showed minimal carbonation that  
308 was limited to the edge of the coupons after 28 days of exposure to CO<sub>2</sub>. This is attributed to the  
309 denser microstructure of Class H cement due to the absence of fly ash and lower water content in  
310 comparison to the WECC and FWECC mixes (Kutchko et al., 2009; Lye et al., 2015; Zhang  
311 and Li, 2013).

312

### 313 **3.2. Effect of carbonation on mechanical integrity of WECC**

314

315 The four-point bending tests carried out on WECC specimens showed that the unreacted  
316 sample exhibited multiple microcracking behavior and significant ductility. The reaction of  
317 WECC specimens with CO<sub>2</sub> impacted the ductility of ECC negatively, while the ductility of  
318 control samples exposed to N<sub>2</sub> headspace under the same temperature and pressure conditions  
319 remained relatively unaltered over the same period.

320 **Fig. 3a** shows the stress-deflection curves as a function of time for WECC samples exposed  
321 to N<sub>2</sub> headspace. The unreacted WECC and all control samples exposed to N<sub>2</sub> headspace for 2, 7,  
322 14, and 28 days showed deflection in the range of 2.2 to 2.5 mm at the maximum flexural stress  
323 and exhibited multiple cracking at the bottom surface of the coupons. The samples also showed  
324 gradual decrease in stress relative to deflection, subsequent to achieving maximum flexural  
325 strength, which is typical in strain hardening ECC (Mohamed and Li, 1994) rather than a sudden  
326 drop to zero observed in brittle wellbore cement after achieving maximum flexural strength.

327 **Fig. 3b** shows the stress-deflection curves for WECC control samples exposed to CO<sub>2</sub> acidified  
328 water. In contrast to control samples exposed to N<sub>2</sub> headspace, carbonated WECC showed a  
329 significant decline in the total deflection of the specimens, with deflection in the range of 0.5 to  
330 0.8 mm at the ultimate flexural stress. This deflection is approximately one-third of the  
331 deflection of control samples exposed to N<sub>2</sub> headspace. The carbonated samples also exhibited  
332 rapid increase in stress relative to deflection characterized by the increase in the initial slope of  
333 the stress-deflection curve as the extent of carbonation increased. The significant decrease in

334 ductility of WECC and rapid initial increase in stress relative to deflection after carbonation may  
 335 be explained by stiffening and strengthening of the specimen by the combined effects of  
 336 densification of the microstructure of WECC matrix, as reported by Wu et al. (2018), and  
 337 densification of the fiber-matrix interfacial transition zone (ITZ) reported by Adeoye et al.  
 338 (2019) following carbonation. In particular, the densified ITZ increases the interfacial bonding  
 339 between the fiber and the matrix such that the fibers are unable to pullout easily from the matrix  
 340 under flexural stress, leading to fiber rupture and subsequent embrittlement of the composite.

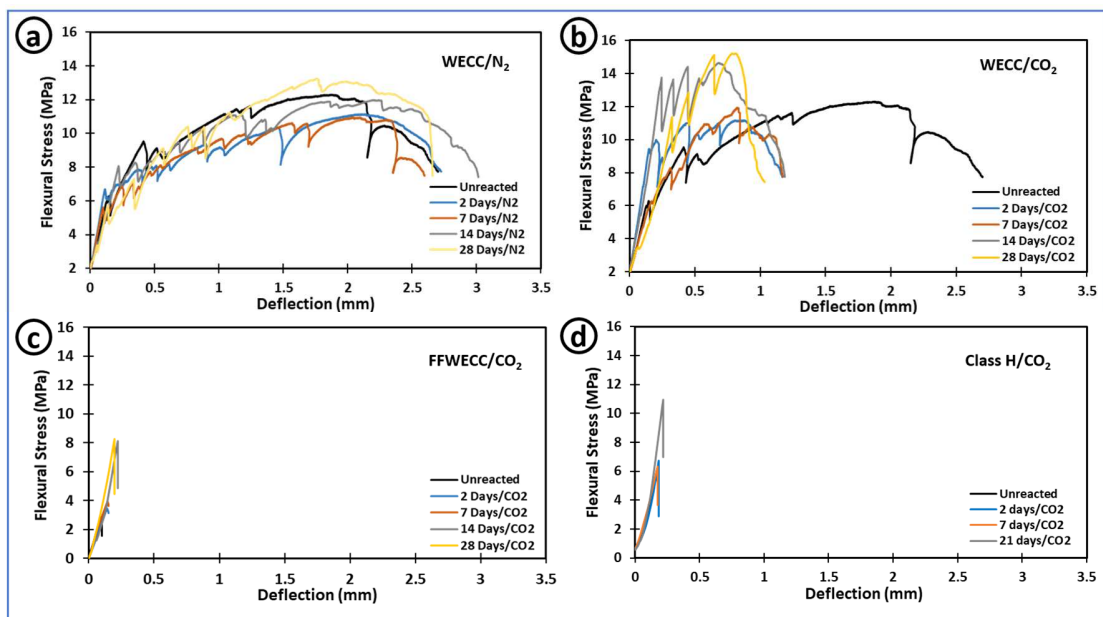


**Fig 3:** Four-point flexural stress-deflection curves for (a) unaltered WECC and carbonated WECC coupons, (b) unaltered WECC and control WECC coupons exposed to N<sub>2</sub> headspace (c) unaltered and carbonated FWECC coupons (d) unaltered and carbonated Class H coupons, under GCS conditions of 50°C and 10 MPa.

341

342

343 **Fig. 3c and Fig. 3d** show the stress-deflection curves of the FWECC and Class H cement  
 344 samples, respectively. In contrast to WECC which exhibited strain hardening and ductility,  
 345 FWECC and Class H samples exhibited brittle failure prior to and after exposure to CO<sub>2</sub>.  
 346 Similar to WECC, we observed an increase in the ultimate flexural strength of FWECC and  
 347 Class H wellbore cement with increased extent of carbonation. The modulus of rupture increased

348 from 2.9 to 8.2 MPa and 6.2 to 10.9 MPa after 28 and 21 days of reaction, for FWECC and  
 349 Class H cement, respectively.

350 **Table 3** presents the ultimate flexural strength, known as the modulus of rupture, for each of  
 351 the materials. It was observed that the ultimate flexural strength for WECC was consistently  
 352 higher than that of FWECC and Class H irrespective of the extent of carbonation of the  
 353 material. Hence, while the carbonation reaction decreased the ductility of WECC, WECC  
 354 continued to exhibit superior ductile performance in comparison to conventional wellbore  
 355 cementing materials under  
 356 typical GCS conditions. In addition, the superior ductility and multiple cracking behavior of the  
 357 unaltered WECC (**Fig. 3a**) and WECC exposed to N<sub>2</sub> headspace (**Fig. 3b**) suggest that ECC can  
 358 potentially be employed for wellbore cementing in other deep geologic environments such as in  
 359 oil and gas wells, in the absence of CO<sub>2</sub>, without deterioration of its long- term strain hardening  
 360 properties.

361

362 **Table 3:** Ultimate flexural strength (modulus of rupture) for specimens as a function of time.

	$\sigma_{fmax}$ unreacted (MPa)	$\sigma_{fmax}$ 2 days (MPa)	$\sigma_{fmax}$ 7 days (MPa)	$\sigma_{fmax}$ 14 days (MPa)	$\sigma_{fmax}$ 21 days (MPa)	$\sigma_{fmax}$ 28 day (MPa)
WECC <sub>CO2</sub>	12.3	11.2	11.9	14.6	NA	15.2
WECC <sub>N2</sub>	12.3	11.1	10.9	11.9	NA	13.2
FWECC <sub>CO2</sub>	2.9	3.5	3.9	8.1	NA	8.2
Class H <sub>CO2</sub>	6.2	6.7	6.3	NA	10.9	NA

363

### 364 3.3. Microhardness and resistance to deformation

365

366 **Fig. 4a and Fig. 4b** present hardness values for WECC and FWECC specimens,  
 367 respectively, pre- and post-reaction with CO<sub>2</sub>. The results indicate that the resistance of WECC  
 368 to deformation was not compromised following reaction with CO<sub>2</sub>-acidified water in comparison  
 369 to FWECC. The average hardness of the WECC composite prior to carbonation was 37.9 ±2.5  
 370 HV/500g. A general increase in hardness, both at the carbonated edge and uncarbonated core of  
 371 the sample, was observed following reaction with CO<sub>2</sub>. The fact that the uncarbonated region  
 372 exhibited an increase in hardness can be explained by the pore refinement due to continuous

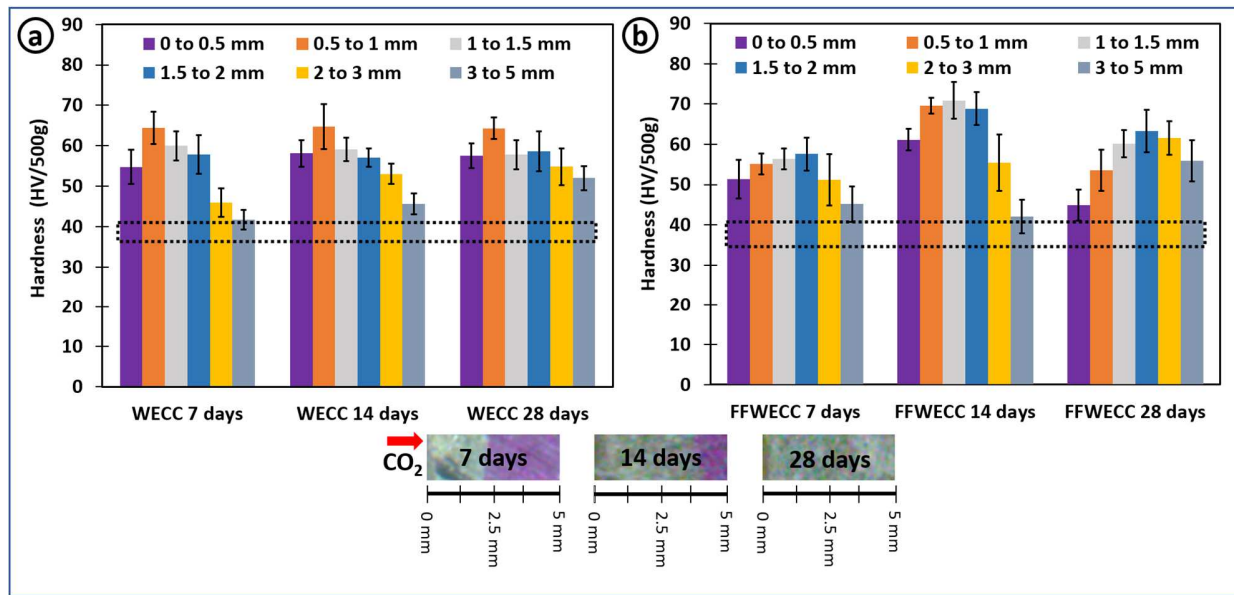


**Fig. 4:** Time-dependent evolution of microhardness for (a) WECC and (b) FFW ECC samples, respectively, following exposure to CO<sub>2</sub> acidified water at 50°C and 10 MPa P<sub>CO<sub>2</sub></sub> for 7, 14, and 28 days. The dotted lines in **Fig. 4a** and **Fig. 4b** represent the range of average hardness for uncarbonated WECC and FFW ECC samples. Picture inserts at the bottom of the figure indicate the extent of post reaction alteration depth associated with both WECC and FFW ECC samples revealed by phenolphthalein pH indicator.

373

374 cement hydration under high temperature and pressure conditions (Adeoye et al., 2019; Kutchko  
 375 et al., 2009; Zhang et al., 2014). For the carbonated region, the highest hardness value was  
 376 observed in the 0.5 to 1.0 mm section of the specimen, indicating that the most substantial pore  
 377 refinement due to carbonation occurred in this region. Although the WECC sample had been  
 378 fully reacted after 28 days of reaction, the sample showed higher microhardness in comparison to  
 379 the unaltered material, indicating that reaction with CO<sub>2</sub> did not negatively alter its resistance to  
 380 deformation. For FFW ECC samples, the average hardness of the material prior to reaction was  
 381 37.6 ±3.0 HV/500g, which was similar to the hardness of the unreacted WECC. Similar to  
 382 WECC, a general increase in the hardness was observed at the core and edge of the FFW ECC  
 383 coupon compared to the unreacted material following exposure to CO<sub>2</sub>. This is attributed to  
 384 continuous coarsening of the matrix microstructure resulting from pozzolanic reactions under  
 385 high temperature and pressure conditions (Adeoye et al., 2019; Zhang et al., 2013). While the  
 386 WECC samples showed the highest hardness at the 0.5 to 1.0 mm zone of the coupon, the  
 387 highest hardness values were measured in the 1.0 to 2.0 mm section of FFW ECC coupons. This

388 is likely due to greater extent of densification at the edge of the carbonated WECC, relative to  
389 the FFW ECC specimens, due to the presence of the PVA fibers. At 28 days of exposure, the  
390 hardness of the FFW ECC specimen was significantly lower at the edge of the coupon than the  
391 hardness of the samples exposed to CO<sub>2</sub> for 14 days. This is most likely due to deterioration of  
392 material at the edge of the sample after prolonged exposure to the CO<sub>2</sub>-acidified water. The fact  
393 that this sharp retrogression in hardness was not observed in WECC samples containing fibers  
394 suggest that the presence of fibers in WECC helped to maintain the structural stability of the  
395 material under the GCS conditions and may help maintain the integrity of the wellbore cement  
396 sheath following acid attack.

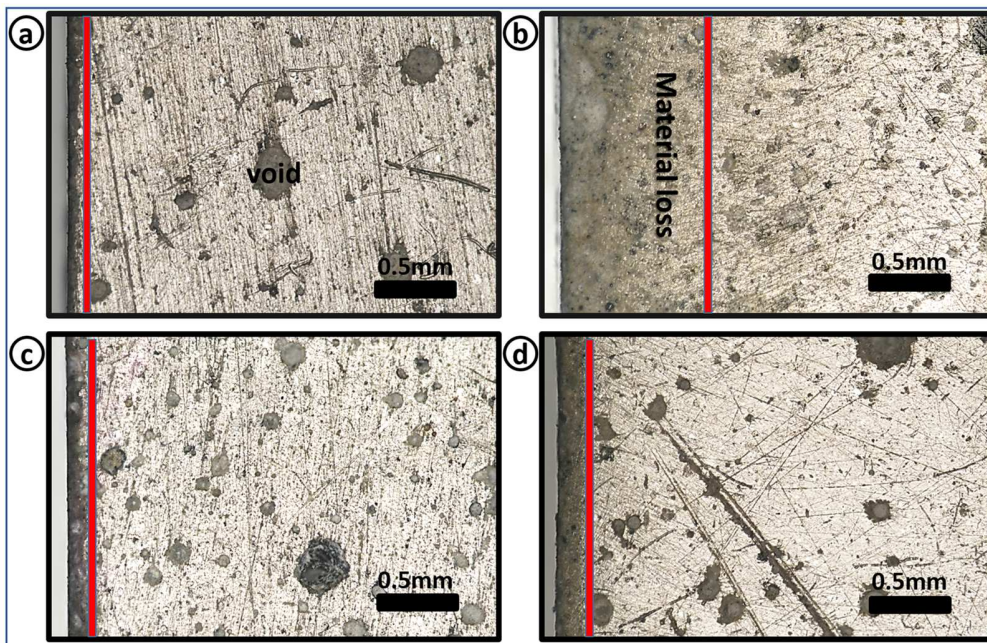


**Fig. 5** Optical image of (a) unaltered FFW ECC coupon (b) FFW ECC coupon after exposure to CO<sub>2</sub> acidified water (c) unaltered WECC coupon, and (d) WECC coupon after exposure to CO<sub>2</sub> acidified water, at temperature and pressure conditions of 50°C and 10 MPa.

414 **Fig. 5a** and **Fig. 5b** show optical images of the edge along the transverse section of the  
415 unaltered FFW ECC coupon and FFW ECC coupon after 28 days of exposure to CO<sub>2</sub> acidified  
416 water, respectively, while **Fig. 5c** and **Fig. 5d** show optical images of the edge of the unreacted  
417 WECC coupon and WECC coupon after 28 days of exposure to CO<sub>2</sub> acidified water. Although  
418 minimal material loss was observed at the edge of WECC samples after 28 days of reaction (**Fig.**

419 **5d)** in comparison to the unreacted sample (**Fig. 5c**), there was significant material loss at the  
420 edge of the FFW ECC specimens in comparison to the unreacted FFW ECC sample. This is  
421 consistent with the surface microhardness result that showed a significant decrease in the  
422 hardness of the FFW ECC samples after 28 days of reaction, supporting the hypothesis that the  
423 presence of  
424 the fibers promoted the long-term structural stability of the composite. This structural stability  
425 and absence of material loss in WECC relative to the FFW ECC is imparted by the microfibers  
426 that helped to bind the matrix together, which will ensure the integrity of the cement sheath and  
427 promote secure storage during GCS.

428

### 429 **3.4. Evolution of compressive strength**

430 **Table 4** presents the average compressive strength for WECC, FFW ECC, and Class H  
431 samples at different time points and exposure conditions. In wellbore cementing, development of  
432 early age compressive strength of the cement ensures both structural support for the casing and  
433 zonal isolation of borehole intervals (Labibzadeh et al., 2010). The recommended compressive  
434 strength of wellbore cement after 24 hours is 3.5 MPa (500 psi) (Labibzadeh et al., 2010; Ridha  
435 et al., 2013). Meeting this target 24 hr compressive strength is crucial for wellbore cement design  
436 in order to limit the wait-on-cement time, i.e. the time between drilling operations, while  
437 ensuring the integrity of the cement job.

438 The results in **Table 4** indicates that the compressive strengths of WECC and FFW ECC were  
439 comparable after 24 hours of curing, although the compressive strength of the WECC was  
440 slightly higher (9.1 MPa) than FFW ECC (8.1 MPa). Class H cement showed considerably higher  
441 compressive strength (13.3 MPa) than both WECC and FFW ECC. After 28 days of curing, the  
442 compressive strength of all sample types increased significantly as expected, with WECC,  
443 FFW ECC, and Class H having compressive strengths of 30, 26.2, and 47.9 MPa, respectively.  
444 The fact that the 24 hr and 28 day compressive strengths of WECC and FFW ECC samples were  
445 consistently lower than that of Class H cement may be due to the high volume of fly ash in  
446 WECC and FFW ECC, up to 50% replacement by mass. Such high-volume substitution of  
447 cement with fly ash has been shown to reduce the overall compressive strength of Portland  
448 cement (Harison et al., 2014; Lam et al., 1998). Additionally, the WECC and FFW ECC

449 specimens contained a higher proportion of water (45% water:solid) in comparison to Class H  
450 specimens (38% water:solid).

451 Following carbonation of the specimens for 7 days, further increase in the compressive  
452 strength of the samples was observed indicating that carbonation of the samples under the  
453 temperature and pressure conditions tested did not compromise the compressive strength of the  
454 specimens. The increase in compressive strength can be linked to the further hydration and pore  
455 refinement of the cementitious materials under higher GCS temperatures and pressures. While  
456 the FFWECC and Class H showed approximately 8% increase in average compressive strength  
457 following carbonation, WECC showed a 30% increase in compressive strength. The difference  
458 between the increase in compressive strength for FFWECC and WECC can be linked to the  
459 strengthening of the WECC composite due to the densification of the fiber matrix interface  
460 following carbonation, which improves the bonding between the fiber and the matrix and  
461 consequently the overall strength of the composite (Adeoye et al., 2019).

462 It is instructive to note that in addition to exhibiting a higher compressive strength  
463 performance in comparison to conventional fly ash amended wellbore cement, this study has  
464 shown that WECC exhibits superior flexural strength and ductility in comparison to FFWECC,  
465 furthering its potential as a candidate for wellbore cementing applications.

466

467 **Table 4:** Compressive strength for WECC, FFWECC, and Class H sample carbonation at early  
468 age, late age, and post carbonation.

Sample	24 hr unreacted	7 days unreacted	7 days carbonated	% post carbonation change
WECC	9.1	30.0	39.2	30.6
FFWECC	8.0	26.2	28.2	7.8
Class H	13.3	47.9	51.5	7.5

469

### 470 3.5. Evolution of WECC pore structure

471 The pore structure of wellbore cement can influence the transport of fluids through the  
472 uncracked material and thus impact its resistance to CO<sub>2</sub> attack. To reveal the evolution of  
473 WECC's pore structure in response to exposure to CO<sub>2</sub>-acidified water, the pore size distribution  
474 curves obtained using MIP are plotted in **Fig. 6a** and **Fig. 6b** for WECC and FFWECC samples,  
475 respectively. As shown in **Fig. 6a**, the total intruded volume in WECC increased from 0.16 mL/g  
476 to 0.19 mL/g following 28 days of carbonation, whereas the total intruded volume for the control  
477 samples exposed to N<sub>2</sub> headspace remained relatively unchanged at 0.15 mL/g. In the absence of

478 fiber, however, the conventional fly ash amended wellbore cementing material (FFWECC)  
 479 showed  
 480 comparable intruded volumes of approximately 0.14 mL/g for the unaltered and carbonated  
 481 samples (see **Fig. 6b**). The total intruded volume for the control FFWECC sample exposed to N<sub>2</sub>  
 482 headspace also remained constant at 0.14 mL/g after 28 days.  
 483

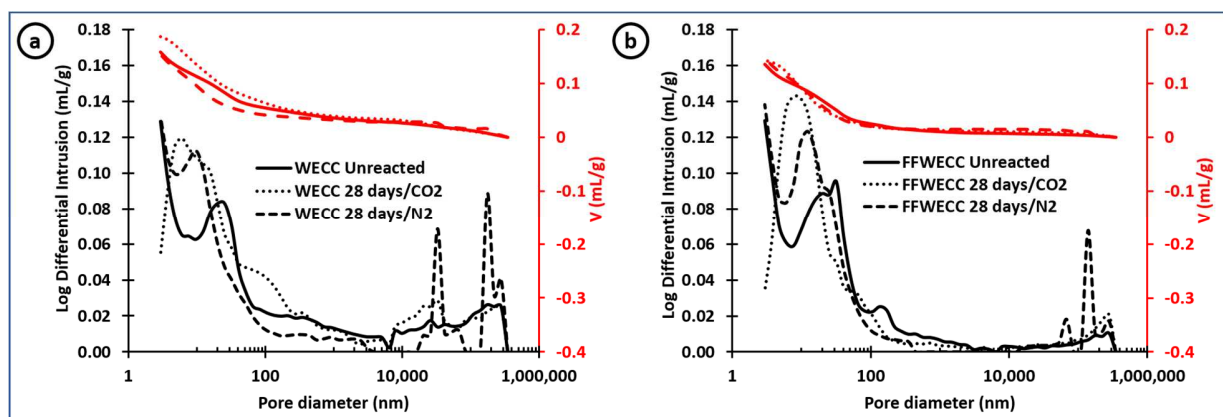


**Fig. 6:** Cumulative and differential pore size distribution for unreacted and altered (a) WECC and (b) FFWECC follow exposure to CO<sub>2</sub> acidified water and N<sub>2</sub> headspace for 28 days at temperature and pressure conditions of 50°C and 10 MPa. The “critical diameter” corresponding pore diameter at the inflection point on the intrusion volume vs. pore diameter curve

484

485 In **Fig. 6**, the “critical diameter” can be visually identified as the pore diameter at the  
 486 maximum inflection point on the intrusion volume vs. pore diameter curve (Aligizaki, 2005;  
 487 Halamickova et al., 1995; Zhang and Shao, 2018). The critical diameter is interpreted as the  
 488 smallest diameter of the subset of the pores that creates a connected path through the composite  
 489 matrix (Berodier and Scrivener, 2015; Halamickova et al., 1995; Nishiyama and Yokoyama,  
 490 2017; Zhang and Shao, 2018), and represents the primary connected pores controlling the fluid  
 491 transport behavior of the composite. The critical pore diameter decreased from approximately 30  
 492 nm in the unreacted specimens, for both WECC (**Fig. 6a**) and FFWECC (**Fig. 6b**), to < 20 nm  
 493 for the control samples exposed to N<sub>2</sub> headspace at a temperature and pressure of 50°C and 10  
 494 MPa. This decrease is likely due to continuous hydration and pore refinement under high  
 495 temperature and pressure conditions. Similarly, carbonation of the samples due to exposure to  
 496 CO<sub>2</sub>-acidified water further decreased the critical pore diameter below 10 nm for both WECC  
 497 (**Fig. 6a**) and FFWECC (**Fig. 6b**) samples. The observation that the post-carbonation critical

498 pore diameters were comparable between the WECC and FWECC samples indicates that the  
 499 incorporation of fibers at 1.1% volume will not increase permeation of fluids through uncracked  
 500 WECC.

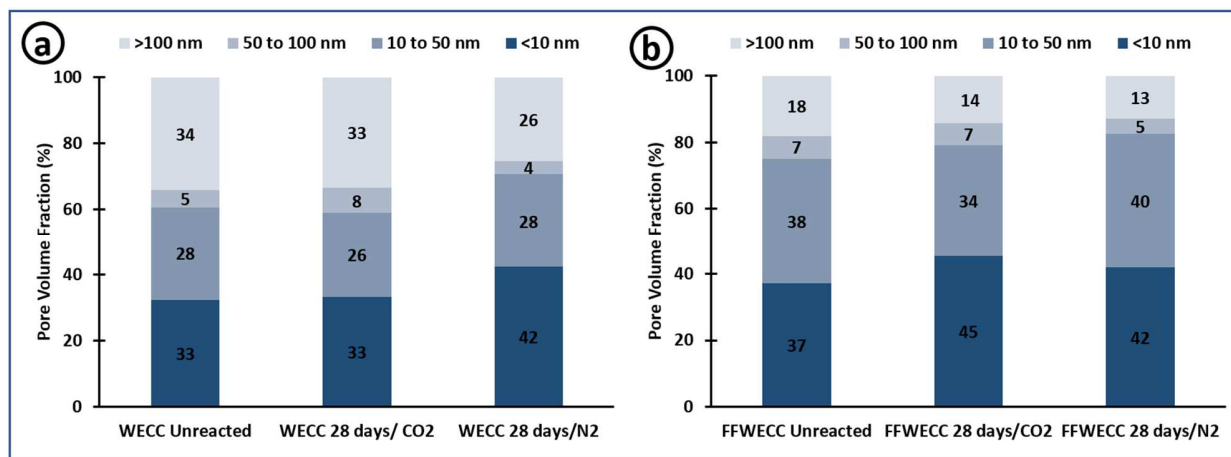


**Fig. 7:** Normalized pore volume fraction distribution for unreacted and altered (a) WECC and (b) FWECC follow exposure to CO<sub>2</sub> acidified water and N<sub>2</sub> headspace for 28 days at temperature and pressure conditions of 50°C and 10 MPa.

501  
 502 To further understand the evolution of pore size based on the intruded volumes and  
 503 differential pore size distribution curves, the total pore volume was divided into four groups  
 504 based on pore diameters: voids (>100 nm), large capillary pores (50-100 nm), medium capillary  
 505 pores (10-50 nm), and gel pores (<10 nm) (Aligizaki, 2005; Zhang and Shao, 2018). The  
 506 normalized volume fraction of each group with respect to the total pore volume is shown in **Fig.**  
 507 **7a and Fig. 7b** for WECC and FWECC, respectively. It was observed that the volume fraction  
 508 of voids (pore diameter >100 nm) doubled when PVA fibers were added to the matrix at 1.1%  
 509 volume in unreacted samples (i.e., for unreacted WECC vs. unreacted FWECC), carbonated  
 510 samples, and samples exposed to N<sub>2</sub>-headspace. In WECC samples, voids made up 34%, 33%,  
 511 and 26% of the pore fraction for unreacted samples, carbonated samples, and samples exposed to  
 512 N<sub>2</sub> headspace, respectively, while the volume fraction of voids in the FWECC samples exposed  
 513 to similar conditions was 18%, 14% and 13%, respectively (**Fig. 7b**). This indicates that the  
 514 presence of the PVA fibers coarsened the pore structure, particularly following exposure to CO<sub>2</sub>-  
 515 acidified water where the volume fraction of voids increased by over 100%.

516 The coarsening of the pore structure following the addition of the PVA fibers can be  
 517 explained by the existence of the fiber-matrix ITZ in WECC. Analogous to the ITZ between the

518 aggregate and cement paste in conventional concrete, a coarser pore structure is potentially  
519 created in the matrix adjacent to fibers due to the “wall effect” that accounts for the increases in  
520 the total pore volume and void fractions when the PVA fibers are incorporated. The volume of  
521 mercury that intruded along the ITZ is interpreted as the volume for the pore size corresponding  
522 to the percolation pressure for the ITZ width. Thus, the presence of the PVA fibers leads to an  
523 increase in the fraction of voids in WECC.

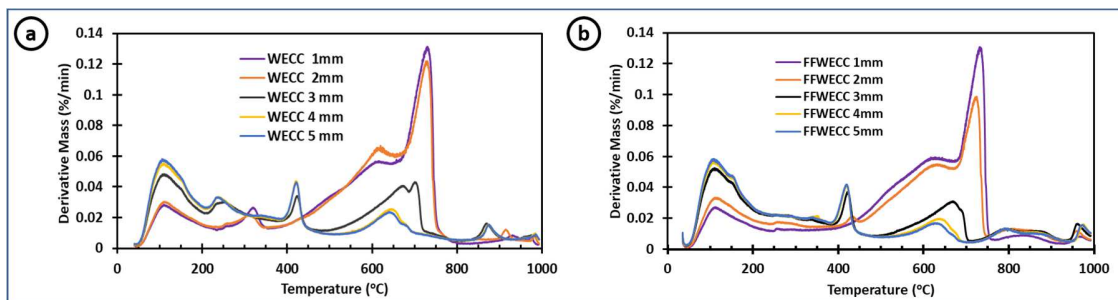


**Fig. 8:** DTG curves for (a). WECC and (b). FWECC specimens at different depths into the carbonated coupons. The result indicates a decrease in the extent of carbonation of the samples with depth and significantly higher extent of carbonation at the 1 to 2 mm section of the sample in comparison to the 3 to 5 mm sections. The trend and extent of carbonation for WECC and FWECC specimens are similar. Note that the 1 mm section is the surface of the sample exposed to the solution while 5 mm section represents the mid-section of the exposed sample.

524

525

526 Despite the increase in fraction of voids observed in WECC samples compared to FWECC  
527 samples, it is interesting that the critical diameter of WECC was similar to that of FWECC  
528 samples. This suggests that the coarsening of WECC porosity due to the presence of the ITZ is  
529 unlikely to impact the material permeability, potentially due to isolated distribution and absence  
530 of interconnectedness of the ITZ compared to the pores in the matrix. Nevertheless, further  
531 investigation is needed to understand the pore structure in WECC using direct observation  
532 techniques, such as high-resolution scanning electron microscopy coupled with backscatter  
533 electron spectroscopy and x-ray scattering, to examine how this physical change of the pore  
534 structure will impact the permeability of WECC to CO<sub>2</sub>-rich fluids under CGS conditions.

535

536 **3.6. Evolution of chemical composition**

537 **Fig. 8a** and **Fig. 8b** present the derivative of thermogravimetric analysis (DTG) curves for  
538 specimens obtained at different depths along the thickness of WECC and FWECC coupons  
539 following exposure to CO<sub>2</sub>-acidified water for 7 days. As presented in the literature, dehydration  
540 of calcium silicate hydrate (C-S-H) occurs from 40 to 200°C, dehydroxylation of portlandite  
541 (Ca(OH)<sub>2</sub>) from 380 to 450°C, and decarbonization of calcium carbonate (CaCO<sub>3</sub>) occurs from  
542 450 to 750°C (Neves Junior et al., 2019, 2015; Sato et al., 2007). Material depths (measured from  
543 the outside edge of the sample) of 1 mm and 2 mm represent the fully reacted zone, the 4 mm  
544 and 5 mm sections represent the unaltered zone, and the 3 mm section is the partially carbonated  
545 zone, for both WECC and FWECC samples (see **Fig. 1d** for schematic). The unaltered 4 mm  
546 and 5 mm sections showed comparable trends, with near overlapping DTG curves and similar  
547 magnitude for C-S-H, Ca(OH)<sub>2</sub>, and CaCO<sub>3</sub>. The 1 mm and 2 mm sections were depleted in  
548 Ca(OH)<sub>2</sub> but showed a significant increase in the intensity of the CaCO<sub>3</sub> peaks as compared to  
549 the unaltered sections and the transition zone, indicating the conversion of Ca(OH)<sub>2</sub> to CaCO<sub>3</sub>.  
550 Similarly, the intensity of the C-S-H peak decreased progressively from the 1 mm to 5mm  
551 section due to partial carbonation of C-S-H.

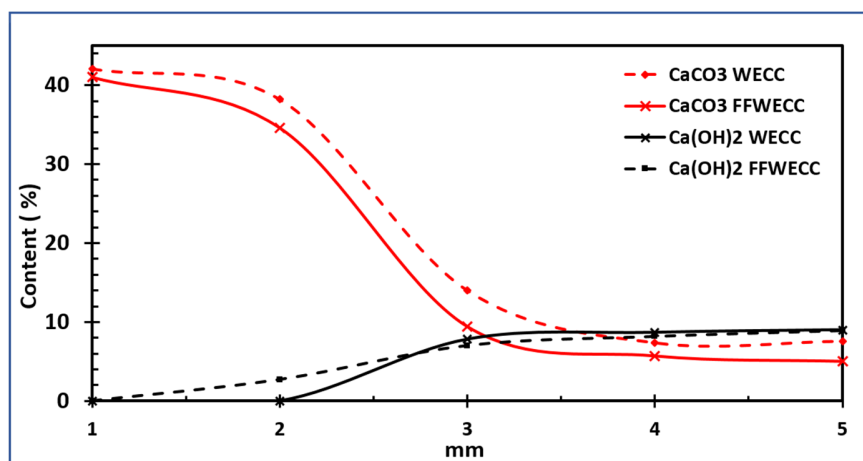


**Fig. 9:** Evolution of CaCO<sub>3</sub> and Ca(OH)<sub>2</sub> content in WECC and FWECC coupons along the reaction front.

552

553

554 For the WECC samples, an additional peak was observed between 225 and 350°C (**Fig. 8a**).  
555 This peak corresponds to the decomposition of the PVA fibers (Panaitescu et al., 2011; Peng et  
556 al., 2017; Zhou et al., 2012), which explains its absence in the FFW ECC specimens. A  
557 progressive shift in the onset of thermal decomposition of PVA fibers can be clearly observed  
558 following carbonation, suggesting that the shift is a consequence of the interaction of the fibers  
559 with CaCO<sub>3</sub>. This may be explained by the nucleation of CaCO<sub>3</sub> on the fibers following  
560 carbonation, as reported by Adeoye et al., (2019), which possibly led to thermal instability of the  
561 fibers. Such shifts in the onset of thermal decomposition, relative to unmodified materials, have  
562 been reported in studies on coated fibers and fibers treated with CaCO<sub>3</sub> (Al-Sabagh et al., 2018;  
563 Bandyopadhyay-Ghosh et al., 2015; Deshmukh et al., 2010; Noor Zuhaira and Rahmah, 2013).

564 **Fig. 9** presents the normalized percentage of CaCO<sub>3</sub> and Ca(OH)<sub>2</sub> relative to the total mass  
565 loss as a function of temperature at different depths for the WECC and FFW ECC specimens. It  
566 can be seen that the CaCO<sub>3</sub> content in the specimens decreased from 41% and 42% in the most  
567 carbonated section to 5% and 7.5% in the unaltered zone for FFW ECC and WECC, respectively.  
568 Similarly, the Ca(OH)<sub>2</sub> content increased from 0% in the fully reacted zone to 8.9% in the  
569 unaltered zone for both FFW ECC and WECC samples. Because the proportion of Ca(OH)<sub>2</sub> in  
570 unaltered cement typically varies from 15 to 20% (Michaux et al., 1990), the fact that the  
571 Ca(OH)<sub>2</sub> content in the uncarbonated core of the WECC and FFW ECC was only 8.9% can be  
572 explained by depletion of the Ca(OH)<sub>2</sub> due to the pozzolanic reaction in the high-volume fly ash  
573 matrix. The most significant change in Ca(OH)<sub>2</sub> and CaCO<sub>3</sub> content occurred between the 2 mm  
574 and 3 mm sections. This mirrors the boundary of the carbonation front as determined by use of  
575 the phenolphthalein solution (**Fig. 2**), demonstrating that the pH indicator captured the depth of  
576 the alteration front well. The absence of sharp spikes or dips in the CaCO<sub>3</sub> content along the  
577 altered zone supports previous studies which showed that exposure to CO<sub>2</sub>-acidified water does  
578 not result in distinct reaction zones in fly ash-amended cementitious materials (Adeoye et al.,  
579 2019; Crow et al., 2010; Zhang et al., 2014), whereas it does in neat Portland cement (Kutchko et  
580 al., 2007). This result also shows that the presence of the fibers will not alter the chemical  
581 gradient in WECC, and its ability to protect the wellbore steel casing will not be significantly  
582 different from that of the conventional fly-ash amended wellbore cement.

583

#### 584 **4. Conclusion**

585 In this study, a novel strain hardening engineered cementitious composite (WECC) designed  
586 for wellbore applications was exposed to CO<sub>2</sub>-acidified water at temperature and pressure  
587 conditions of 50°C and 10 MPa to investigate the effect of carbonation reactions on its overall  
588 mechanical integrity during GCS operations. WECC is proposed here for use in primary  
589 cementing of wellbores during GCS because it exhibits tensile ductility superior to conventional  
590 wellbore cement and has the potential to prevent damage to the cement sheath caused by stresses  
591 from casing expansion/contraction due to thermal swings during CO<sub>2</sub> injection. The results  
592 showed that although the tensile ductility of WECC will decrease following exposure to CO<sub>2</sub>-  
593 acidified water, it will continue to maintain superior ductility in comparison to conventional  
594 wellbore cements under similar conditions. The incorporation of PVA fibers in WECC was  
595 found to prevent retrogression of the material hardness, which was not the case for fiber-free  
596 conventional fly ash-amended wellbore cement. It was also found that the fibers did not promote  
597 deeper depth of CO<sub>2</sub> penetration, as WECC exhibited similar depths of carbonation to that of  
598 conventional fly ash-amended wellbore cement at the different time points investigated. Porosity  
599 and pore size distribution analysis using MIP analysis showed that while the incorporation of  
600 fibers increased the proportion of voids in WECC, which was attributed to the presence of the  
601 fiber/matrix interface, its overall porosity and critical pore diameter trend was similar to that of  
602 fly ash-amended cement. This suggests that the fiber/matrix ITZ will not form a continuous  
603 conductive pathway and PVA fibers in WECC will not change its permeability significantly in  
604 comparison to fly ash-amended wellbore cement. Overall, the high durability exhibited by the  
605 novel fiber-reinforced WECC after exposure to CO<sub>2</sub>-acidified water may make this material a  
606 viable candidate for wellbore cementing applications that aim to prevent cracking of the cement  
607 sheath and mitigate upward leakage of stored fluids such as supercritical CO<sub>2</sub>.

608

#### 609 **Acknowledgement**

610 The authors acknowledge partial funding support from the U.S. Department of Energy through  
611 grant DE-FE0030684. J. T. Adeoye received partial funding support through the University of  
612 Michigan Rackham Predoctoral Fellowship Program.

613

#### 614 **References**

615 Adeoye, J.T., Beversluis, C., Murphy, A., Li, V.C., Ellis, B.R., 2019. Physical and chemical alterations in  
616 engineered cementitious composite under geologic CO<sub>2</sub> storage conditions. *Int. J. Greenh. Gas*  
617 *Control* 83, 282–292. <https://doi.org/10.1016/j.ijggc.2019.01.025>

618 Aligizaki, K.K., 2005. *Pore Structure of Cement-Based Materials : Testing, Interpretation and*  
619 *Requirements*. CRC Press. <https://doi.org/10.1201/9781482271959>

620 Al-Sabagh, A.M., Abdou, M.I., Migahed, M.A., Fadl, A.M., El-Shahat, M.F., 2018. Influence of surface  
621 modified nanoilmelite/amorphous silica composite particles on the thermal stability of cold  
622 galvanizing coating. *Egypt. J. Pet.* 27, 137–144. <https://doi.org/10.1016/j.ejpe.2017.02.002>

623 ASTM, 2016. *Test Method for Compressive Strength of Hydraulic Cement Mortars (Using 2-in. or [50-*  
624 *mm] Cube Specimens)*. ASTM International. [https://doi.org/10.1520/C0109\\_C0109M-16A](https://doi.org/10.1520/C0109_C0109M-16A)

625 ASTM, 2012. *C1609/C1609M-12. Test Method for Flexural Performance of Fiber-Reinforced Concrete*  
626 *(Using Beam With Third-Point Loading)*. ASTM International.  
627 [https://doi.org/10.1520/C1609\\_C1609M-12](https://doi.org/10.1520/C1609_C1609M-12)

628 Bachu, S., Celia, M.A., 2009. Assessing the potential for CO<sub>2</sub> leakage, particularly through wells, from  
629 geological storage sites, in: *Geophysical Monograph Series*. Am. Geophys. Union Wash. C Pp  
630 203–216.

631 Bandyopadhyay-Ghosh, S., Ghosh, S.B., Sain, M., 2015. 19 - The use of biobased nanofibres in  
632 composites, in: Faruk, O., Sain, Mohini (Eds.), *Biofiber Reinforcements in Composite Materials*.  
633 Woodhead Publishing, pp. 571–647. <https://doi.org/10.1533/9781782421276.5.571>

634 Barlet-Gouédard, V., Rimmelé, G., Goffé, B., Porcherie, O., 2007. Well Technologies for CO<sub>2</sub> Geological  
635 Storage: CO<sub>2</sub>-Resistant Cement. *Oil Gas Sci. Technol. - Rev. IFP* 62, 325–334.  
636 <https://doi.org/10.2516/ogst:2007027>

637 Berodier, E., Scrivener, K., 2015. Evolution of pore structure in blended systems. *Cem. Concr. Res.* 73,  
638 25–35. <https://doi.org/10.1016/j.cemconres.2015.02.025>

639 Cao, P., Karpyn, Z.T., Li, L., 2015. Self-healing of cement fractures under dynamic flow of CO<sub>2</sub>-rich brine.  
640 *Water Resour. Res.* 51, 4684–4701. <https://doi.org/10.1002/2014WR016162>

641 Carroll, S., Carey, J.W., Dzombak, D., Huerta, N.J., Li, L., Richard, T., Um, W., Walsh, S.D.C., Zhang, L.,  
642 2016. Review: Role of chemistry, mechanics, and transport on well integrity in CO<sub>2</sub> storage  
643 environments. *Int J Greenh Gas Control* 49, 149–160.  
644 <https://doi.org/10.1016/j.ijggc.2016.01.010>

645 Cheshire, M.C., Stack, A.G., Carey, J.W., Anovitz, L.M., Prisk, T.R., Ilavsky, J., 2017. Wellbore Cement  
646 Porosity Evolution in Response to Mineral Alteration during CO<sub>2</sub> Flooding. *Environ. Sci. Technol.*  
647 51, 692–698. <https://doi.org/10.1021/acs.est.6b03290>

648 Chow, J.C., Watson, J.G., Herzog, A., Benson, S.M., Hidy, G.M., Gunter, W.D., Penkala, S.J., White, C.M.,  
649 2003. Separation and Capture of CO<sub>2</sub> from Large Stationary Sources and Sequestration in  
650 Geological Formations. *J. Air Waste Manag Assoc* 53, 1172–1182.  
651 <https://doi.org/10.1080/10473289.2003.10466274>

652 Crow, W., Carey, J.W., Gasda, S., Brian Williams, D., Celia, M., 2010. Wellbore integrity analysis of a  
653 natural CO<sub>2</sub> producer. *Int. J. Greenh. Gas Control, The Ninth International Conference on*  
654 *Greenhouse Gas Control Technologies* 4, 186–197. <https://doi.org/10.1016/j.ijggc.2009.10.010>

655 Deel, D., 2007. *Carbon Sequestration Technology Roadmap and Program Plan* 2007 48.

656 Deshmukh, G.S., Pathak, S.U., Peshwe, D.R., Ekhe, J.D., 2010. Effect of uncoated calcium carbonate and  
657 stearic acid coated calcium carbonate on mechanical, thermal and structural properties of  
658 poly(butylene terephthalate) (PBT)/calcium carbonate composites. *Bull. Mater. Sci.* 33, 277–284.  
659 <https://doi.org/10.1007/s12034-010-0043-7>

660 Dieter, G.E., Bacon, D.J., 1986. *Mechanical metallurgy*. McGraw-hill New York.

661 Fabbri, A., Corvisier, J., Schubnel, A., Brunet, F., Goffé, B., Rimmelé, G., Barlet-Gouédard, V., 2009. Effect  
662 of carbonation on the hydro-mechanical properties of Portland cements. *Cem* 39, 1156–1163.  
663 <https://doi.org/10.1016/j.cemconres.2009.07.028>

664 Feldman, R.F., 1987. Diffusion measurements in cement paste by water replacement using Propan-2-OL.  
665 *Cem. Concr. Res.* 17, 602–612. [https://doi.org/10.1016/0008-8846\(87\)90133-5](https://doi.org/10.1016/0008-8846(87)90133-5)

666 Gallé, C., 2001. Effect of drying on cement-based materials pore structure as identified by mercury  
667 intrusion porosimetry: A comparative study between oven-, vacuum-, and freeze-drying. *Cem.*  
668 *Concr. Res.* 31, 1467–1477. [https://doi.org/10.1016/S0008-8846\(01\)00594-4](https://doi.org/10.1016/S0008-8846(01)00594-4)

669 Guillot, D., 1990. Rheology of Well Cement Slurries, in: Nelson, E.B. (Ed.), *Developments in Petroleum*  
670 *Science, Well Cementing*. Elsevier, pp. 4–1. [https://doi.org/10.1016/S0376-7361\(09\)70302-4](https://doi.org/10.1016/S0376-7361(09)70302-4)

671 Halamickova, P., Detwiler, R.J., Bentz, D.P., Garboczi, E.J., 1995. Water permeability and chloride ion  
672 diffusion in portland cement mortars: Relationship to sand content and critical pore diameter.  
673 *Cem. Concr. Res.* 25, 790–802. [https://doi.org/10.1016/0008-8846\(95\)00069-0](https://doi.org/10.1016/0008-8846(95)00069-0)

674 Harison, A., Srivastava, V., Herbert, A., 2014. Effect of Fly Ash on Compressive Strength of Portland  
675 Pozzolona Cement Concrete 2, 4.

676 Huerta, N.J., Hesse, M.A., Bryant, S.L., Strazisar, B.R., Lopano, C., 2016. Reactive transport of CO<sub>2</sub>-  
677 saturated water in a cement fracture: Application to wellbore leakage during geologic CO<sub>2</sub>  
678 storage. *Int. J. Greenh. Gas Control* 44, 276–289. <https://doi.org/10.1016/j.ijggc.2015.02.006>

679 IPCC, Metz, B. (Eds.), 2005. IPCC special report on carbon dioxide capture and storage. Cambridge  
680 University Press, for the Intergovernmental Panel on Climate Change, Cambridge.

681 Jen, C.-P., Li, C., Zhang, K., 2017. Effects of Injection Pressure on Geological CO<sub>2</sub> Storage in the  
682 Northwest Taiwan Basin. *Aerosol Air Qual. Res.* 17, 1033–1042.  
683 <https://doi.org/10.4209/aaqr.2016.12.0526>

684 Kan, Shi, H. -s., Sakulich, A.R., Li, V.C., 2010. Self-Healing Characterization of Engineered Cementitious  
685 Composite Materials. *ACI Mater* 107, 617–624.

686 Kutchko, B.G., Strazisar, B.R., Dzombak, D.A., Lowry, G.V., Thaulow, N., 2007. Degradation of Well  
687 Cement by CO<sub>2</sub> under Geologic Sequestration Conditions. *Env. Sci Technol* 41, 4787–4792.  
688 <https://doi.org/10.1021/es062828c>

689 Kutchko, B.G., Strazisar, B.R., Huerta, N., Lowry, G.V., Dzombak, D.A., Thaulow, N., 2009. CO<sub>2</sub> Reaction  
690 with Hydrated Class H Well Cement under Geologic Sequestration Conditions: Effects of Flyash  
691 Admixtures. *Env. Sci* 43, 3947–3952. <https://doi.org/10.1021/es803007e>

692 Labibzadeh, M., Zahabizadeh, B., Khajehdezfuly, A., 2010. Early-age compressive strength assessment of  
693 oil well class G cement due to borehole pressure and temperature changes 10.

694 Lam, L., Wong, Y.L., Poon, C.S., 1998. Effect of Fly Ash and Silica Fume on Compressive and Fracture  
695 Behaviors of Concrete. *Cem. Concr. Res.* 28, 271–283. [https://doi.org/10.1016/S0008-8846\(97\)00269-X](https://doi.org/10.1016/S0008-8846(97)00269-X)

696

697 Li, Q., Lim, Y.M., Flores, K.M., Kranjc, K., Jun, Y.-S., 2015. Chemical Reactions of Portland Cement with  
698 Aqueous CO<sub>2</sub> and Their Impacts on Cement's Mechanical Properties under Geologic CO<sub>2</sub>  
699 Sequestration Conditions. *Env. Sci Technol* 49, 6335–6343. <https://doi.org/10.1021/es5063488>

700 Li, V., Wu, C., Wang, S., Ogawa, A., Saito, T., 2002. Interface Tailoring for Strain-Hardening Polyvinyl  
701 Alcohol-Engineered Cementitious Composite (PVA-ECC). *ACI Mater. J.* 99.  
702 <https://doi.org/10.14359/12325>

703 Li, V.C., 2009. Engineered Cementitious Composites (ECC) – material, structural and durability  
704 performance, in: *Concrete Construction Engineering Handbook*. CRC Press, Boca Raton.

705 Li, V.C., 2003. On engineered cementitious composites (ECC). *J Adv* 1, 215–230.

706 Lye, C.-Q., Dhir, R.K., Ghataora, G.S., 2015. Carbonation resistance of fly ash concrete. *Mag. Concr. Res.*  
707 67, 1150–1178. <https://doi.org/10.1680/macr.15.00204>

708 Michaux, M., Nelson, E.B., Vidick, B., 1990. 2 Chemistry and Characterization of Portland Cement, in:  
709 Nelson, E.B. (Ed.), *Developments in Petroleum Science, Well Cementing*. Elsevier, pp. 2–1.  
710 [https://doi.org/10.1016/S0376-7361\(09\)70300-0](https://doi.org/10.1016/S0376-7361(09)70300-0)  
711 Mohamed, M., Li, V.C., 1994. Flexural/Tensile-Strength Ratio in Engineered Cementitious Composites. *J.*  
712 *Mater. Civ. Eng.* 6, 513–528. [https://doi.org/10.1061/\(ASCE\)0899-1561\(1994\)6:4\(513\)](https://doi.org/10.1061/(ASCE)0899-1561(1994)6:4(513))  
713 Nelson, E.B., 1990. *Well Cementing*. Newnes.  
714 Nelson, E.B., Baret, J.-F., Michaux, M., 1990. 3 Cement Additives and Mechanisms of Action, in: Nelson,  
715 E.B. (Ed.), *Developments in Petroleum Science, Well Cementing*. Elsevier, pp. 3–1.  
716 [https://doi.org/10.1016/S0376-7361\(09\)70301-2](https://doi.org/10.1016/S0376-7361(09)70301-2)  
717 Neves Junior, A., Dweck, J., Filho, R.D.T., Ellis, B., Li, V., 2019. Determination of CO<sub>2</sub> capture during  
718 accelerated carbonation of engineered cementitious composite pastes by thermogravimetry. *J.*  
719 *Therm. Anal. Calorim.* <https://doi.org/10.1007/s10973-019-08210-y>  
720 Neves Junior, A., Toledo Filho, R.D., de Moraes Rego Fairbairn, E., Dweck, J., 2015. The effects of the  
721 early carbonation curing on the mechanical and porosity properties of high initial strength  
722 Portland cement pastes. *Constr. Build. Mater.* 77, 448–454.  
723 <https://doi.org/10.1016/j.conbuildmat.2014.12.072>  
724 Neville, A.M., 2011. *Properties of concrete*, 5th ed. ed. Pearson, Harlow, England ; New York.  
725 Nishiyama, N., Yokoyama, T., 2017. Permeability of porous media: Role of the critical pore size. *J.*  
726 *Geophys. Res. Solid Earth* 122, 6955–6971. <https://doi.org/10.1002/2016JB013793>  
727 Noor Zuhaira, A.A., Rahmah, M., 2013. Effect of Calcium Carbonate on Thermal Properties of  
728 CaCO<sub>3</sub>/Kenaf/HDPE and CaCO<sub>3</sub>/Rice Husk/HDPE Composites. *Adv. Mater. Res.* 812, 175–180.  
729 <https://doi.org/10.4028/www.scientific.net/AMR.812.175>  
730 Nordbotten, J.M., Celia, M.A., Bachu, S., Dahle, H.K., 2005. Semianalytical Solution for CO<sub>2</sub> Leakage  
731 through an Abandoned Well. *Environ. Sci. Technol.* 39, 602–611.  
732 <https://doi.org/10.1021/es035338i>  
733 Nordbotten, J.M., Kavetski, D., Celia, M.A., Bachu, S., 2009. Model for CO<sub>2</sub> Leakage Including Multiple  
734 Geological Layers and Multiple Leaky Wells. *Environ. Sci. Technol.* 43, 743–749.  
735 <https://doi.org/10.1021/es801135v>  
736 Panaitescu, D., Frone, A., Ghiurea, M., Spataru, C., Radovici, C., Iorga, M., 2011. Properties of Polymer  
737 Composites with Cellulose Microfibrils, in: *Advances in Composite Materials: Ecodesign and*  
738 *Analysis*. BoD – Books on Demand.  
739 Peng, S., Zhou, M., Liu, F., Zhang, C., Liu, X., Liu, J., Zou, L., Chen, J., 2017. Flame-retardant polyvinyl  
740 alcohol membrane with high transparency based on a reactive phosphorus-containing  
741 compound. *R. Soc. Open Sci.* 4, 170512. <https://doi.org/10.1098/rsos.170512>  
742 Redon, C., Li, V.C., Wu, C., Hoshiro, H., Saito, T., Ogawa, A., 2001. Measuring and Modifying Interface  
743 Properties of PVA Fibers in ECC Matrix. *J. Mater. Civ. Eng.* 13, 399–406.  
744 [https://doi.org/10.1061/\(ASCE\)0899-1561\(2001\)13:6\(399\)](https://doi.org/10.1061/(ASCE)0899-1561(2001)13:6(399))  
745 Ridha, S., Irawan, S., Ariwahjoedi, B., 2013. Strength prediction of Class G oilwell cement during early  
746 ages by electrical conductivity. *J. Pet. Explor. Prod. Technol.* 3, 303–311.  
747 <https://doi.org/10.1007/s13202-013-0075-9>  
748 RILEM, 1984. CPC-18 Measurement of hardened concrete carbonation depth.  
749 Rimmelé, G., Barlet-Gouédard, V., Porcherie, O., Goffé, B., Brunet, F., 2008. Heterogeneous porosity  
750 distribution in Portland cement exposed to CO<sub>2</sub>-rich fluids. *Cem. Concr. Res.* 38, 1038–1048.  
751 <https://doi.org/10.1016/j.cemconres.2008.03.022>  
752 Roy, P., Morris, J.P., Walsh, S.D.C., Iyer, J., Carroll, S., 2018. Effect of thermal stress on wellbore integrity  
753 during CO<sub>2</sub> injection. *Int. J. Greenh. Gas Control* 77, 14–26.  
754 <https://doi.org/10.1016/j.ijggc.2018.07.012>

755 Rutqvist, J., Birkholzer, J., Cappa, F., Tsang, C.-F., 2007. Estimating maximum sustainable injection  
756 pressure during geological sequestration of CO<sub>2</sub> using coupled fluid flow and geomechanical  
757 fault-slip analysis. *Energy Convers. Manag.* 48, 1798–1807.  
758 <https://doi.org/10.1016/j.enconman.2007.01.021>

759 Sato, T., Beaudoin, J.J., Ramachandran, V.S., Mitchell, L.D., Tumidajski, P.J., 2007. Thermal  
760 decomposition of nanoparticulate Ca(OH)<sub>2</sub>-anomalous effects. *Adv. Cem. Res.* 19, 1–7.  
761 <https://doi.org/10.1680/adcr.2007.19.1.1>

762 Spycher, N., Pruess, K., 2005. CO<sub>2</sub>-H<sub>2</sub>O mixtures in the geological sequestration of CO<sub>2</sub>. II. Partitioning in  
763 chloride brines at 12–100°C and up to 600 bar. *Geochim. Cosmochim. Acta* 69, 3309–3320.  
764 <https://doi.org/10.1016/j.gca.2005.01.015>

765 Verbeck, G., 1958. Carbonation of Hydrated Portland Cement, in: Committee C-1, Committee C-9 (Eds.),  
766 Cement and Concrete. ASTM International, 100 Barr Harbor Drive, PO Box C700, West  
767 Conshohocken, PA 19428-2959, pp. 17–17–20. <https://doi.org/10.1520/STP39460S>

768 Watson, T.L., Bachu, S., 2009. Evaluation of the Potential for Gas and CO<sub>2</sub> Leakage Along Wellbores. *SPE*  
769 *Drill* 24, 115–126. <https://doi.org/10.2118/106817-PA>

770 Wu, H.-L., Zhang, D., Ellis, B.R., Li, V.C., 2018. Development of reactive MgO-based Engineered  
771 Cementitious Composite (ECC) through accelerated carbonation curing. *Constr. Build. Mater.*  
772 191, 23–31. <https://doi.org/10.1016/j.conbuildmat.2018.09.196>

773 Zhang, D., Shao, Y., 2018. Surface scaling of CO<sub>2</sub>-cured concrete exposed to freeze-thaw cycles. *J. CO<sub>2</sub>*  
774 *Util.* 27, 137–144. <https://doi.org/10.1016/j.jcou.2018.07.012>

775 Zhang, D., Shao, Y., 2016. Early age carbonation curing for precast reinforced concretes. *Constr. Build.*  
776 *Mater.* 113, 134–143. <https://doi.org/10.1016/j.conbuildmat.2016.03.048>

777 Zhang, L., Dzombak, D.A., Nakles, D.V., Hawthorne, S.B., Miller, D.J., Kutchko, B.G., Lopano, C.L.,  
778 Strazisar, B.R., 2014. Rate of H<sub>2</sub>S and CO<sub>2</sub> attack on pozzolan-amended Class H well cement  
779 under geologic sequestration conditions. *Int. J. Greenh. Gas Control* 27, 299–308.  
780 <https://doi.org/10.1016/j.ijggc.2014.02.013>

781 Zhang, L., Dzombak, D.A., Nakles, D.V., Hawthorne, S.B., Miller, D.J., Kutchko, B.G., Lopano, C.L.,  
782 Strazisar, B.R., 2013. Characterization of pozzolan-amended wellbore cement exposed to CO<sub>2</sub>  
783 and H<sub>2</sub>S gas mixtures under geologic carbon storage conditions. *Int. J. Greenh. Gas Control* 19,  
784 358–368. <https://doi.org/10.1016/j.ijggc.2013.09.004>

785 Zhang, P., Li, Q.-F., 2013. Combined effect of polypropylene fiber and silica fume on workability and  
786 carbonation resistance of concrete composite containing fly ash. *Proc. Inst. Mech. Eng. Part J.*  
787 *Mater. Des. Appl.* 227, 250–258. <https://doi.org/10.1177/1464420712458198>

788 Zhou, K., Jiang, S., Bao, C., Song, L., Wang, B., Tang, G., Hu, Y., Gui, Z., 2012. Preparation of poly(vinyl  
789 alcohol) nanocomposites with molybdenum disulfide (MoS<sub>2</sub>): structural characteristics and  
790 markedly enhanced properties. *RSC Adv.* 2, 11695–11703. <https://doi.org/10.1039/C2RA21719H>

791